Efficiency of buried permanent magnet type 5kW and 50kW high-speed bearingless motors with 4-pole motor windings and 2-pole suspension windings

Rafal P. JASTRZEBSKI*,[a], Pekko JAATINEN*,[b], Akira CHIBA**,[c], Olli PYRHÖNEN*,[d]

*Dept. of Electrical Engineering, Lappeenranta University of Technology, 53851 Lappeenranta, Finland

** Tokyo Institute of Technology, Tokyo, Japan

E-mail: [a]Rafal.Jastrzebski@lut.fi, [b]Pekko.Jaatinen@lut.fi, [c]chiba@ee.titech.ac.jp, [d]Olli.Pyrhonen@lut.fi

Abstract

This work focuses on loss prediction for varying operation conditions of the high-speed buried-type interior permanent magnet (IPM) bearingless motors. The investigated motors are 5 kW and 50 kW units configured as twin motor sets, which provide radial suspension and motoring in 5 degrees of freedom levitated rotor systems with the maximum speed of 30000 r/min. The maximum output power of studied rotor systems is 10 kW and 100kW, respectively. Additionally, the power factors of motor and suspension windings as well as inductance maps for various operating conditions are studied. The magnetic field 2-dimentional transient section analysis and time stepping are applied. The selected results are compared with the measured values. In the loss calculation various rotor and stator iron losses, resistive losses, windage losses and additional losses are taken into account. Efficiency maps and power factor estimation are valuable for application of electrical machines. These studies have been performed using various methods for classical motors and generators but are uncommon for bearingless motors working with different loading conditions. The comprehensive efficiency map prediction of the high-speed IPM bearingless motors for different suspension loading is presented for the first time. The variations of motor inductances for different rotor angles and current amplitudes are derived. The differences in results between the machines with the same geometry but different power are discussed.

Keywords : High-speed electrical machines, Bearingless motor, Self-bearing machine, Energy efficient motor, Permanent magnet motor, Magnetic levitation, Total efficiency, Efficiency map, Losses.

1. Introduction

High-speed permanent magnet (PM) machines are used in many special applications due to their high energy density, robust construction, and high efficiency characteristics. The additional benefits of oil-free operation, infrequent maintenance, build in monitoring, noise reduction, and precise position control can be achieved by applying active magnetic bearings (AMBs). The bearingless motors can be applied to replace the traditional AMBs for contactless and lubrication free support of high-speed rotors. The set of two bearingless motors with the addition of an axial bearing can provide 5-degrees of freedom (5-DOF) suspension to the rotating system. This results in a potentially shorter and lighter rotor, smaller machine footprint, less complex power and control electronics and more integrated control system. When considering industrial feasibility of higher power bearingless motors the prediction on efficiency and power factor in wider operational range is of significant interest.

In-depth losses analysis in high-speed PM machines has been extensively studied in many publications, e.g. (Huynh et al., 2009). At the same time, there have been very little studies concerning efficiency of the bearingless motors in wide power, speed and load range and how the magnetic suspension load affects the efficiency. In majority, low-power applications up to about 1kW with efficiencies studied for very limited conditions have been presented (Yajima, et al., 2007), (Asama et al., 2012), (Steinert et al., 2014). Sinervo and Arkkio (2014) discussed losses for 30 kW 3000 r/min bearingless machine but with suspension only used to produce rotor damping. Sinervo and Arkkio (2014) discussed that in the case of the bearingless induction motor the built in suspension would significantly affect the total efficiency. Some measurements of the efficiency maps of the deeply buried PM bearingless motor with 2-pole motor and 4-pole suspension windings have been presented by Yajima, et al., (2007) but no high-speed operation have been considered. Notably Munteanu et al. (2011) presented the loss measurement of a 40 kW 40000 r/min PM bearingless motor but only for limited

operating conditions.

This work studies losses prediction for varying operation conditions of the high-speed buried-type interior permanent magnet (IPM) bearingless motors. The comprehensive total efficiency maps and power factor maps are constructed. The investigated motors are two twin units, which provide radial suspension in 5-DOF levitated rotor systems with the maximum speed of 30000 r/min and maximum output power of 10 kW and 100 kW, respectively. The performance and scalability of IPM type high-speed bearingless motors are investigated. The introduction of the suspension loading up to three times the needed gravitational load causes negligible effect on total efficiency of studied IPM bearingless motors.

2. Prototype description and rotor structure

The first prototype comprises two 5 kW IPM bearingless motors for radial suspension and torque generation and an axial AMB in between the both motors. Figure 1 shows the Timoshenko beam model of the rotor and its cross section as in finite element method (FEM) analysis. To achieve the required levitation force, a configuration of 2-pole suspension windings and 4-pole motor windings is used. The rotor laminations hold 4 PM poles where each pole comprises 4 magnet segments yielding 16 magnet segments in total and 4 gaps in between the poles per motor. Jaatinen et al. (2015) have presented optimization of this geometry. The total rotor weight is 5.5 kg.

The second prototype is an upscale unit comprising two 50kW IPM bearingless motors and the axial AMB (Fig. 2). Jastrzebski et al. (2015) have presented its electromagnetic design, mechanical stress analysis, rotor dynamics, effect of stator skew, and harmonic spectral analysis. This design employs a winding step shortening with 4/6 pitched motor winding and 5/6 pitched suspension winding. The 15° stator skew is introduced. The total rotor weight is 11.2 kg.

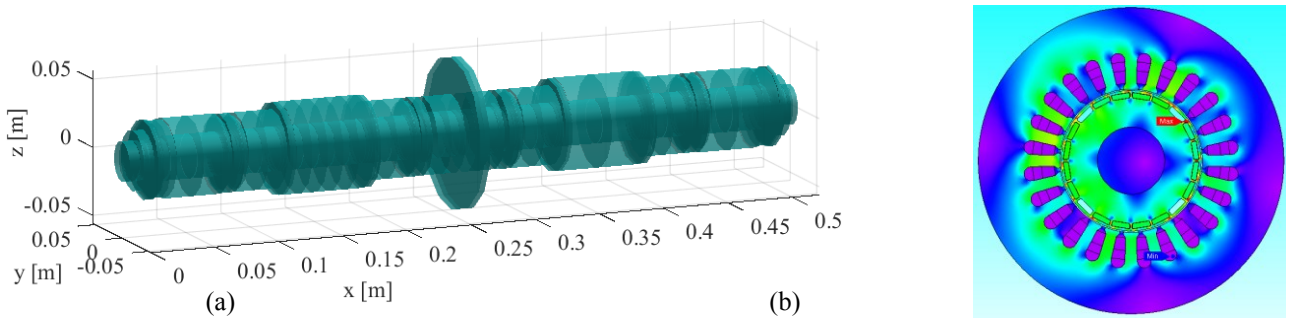

Fig. 1 (a) Rotor dynamic FEM model of 10kW prototype comprising two 5kW motor units and axial AMB. The first free bending modes of the rotor are at 528 Hz, 1069 Hz and 2884 Hz. (b) Electromagnetic 2D FEM model of the motor.

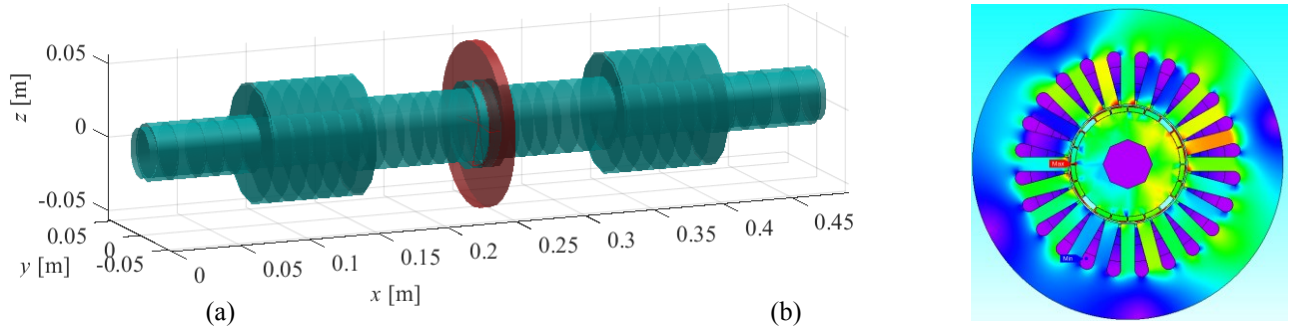

Fig. 2 (a) Rotor dynamic FEM model of 100 kW prototype comprising two 50 kW motor units and axial AMB. The first free bending modes of the rotor are at 1029 Hz, 2675 Hz and 4359 Hz. (b) Electromagnetic 2D FEM model.

3. Estimation of losses and power factors

Typically, if the analytical estimation of losses for an electrical machine is required in complete operational range the solutions are based on static field analysis and extrapolated for wider operating range. In the case of the bearingless motors where there are two interacting rotating electromagnetic fields in different loading conditions, the total loss calculation requires higher computational effort. First, the multiple transient simulations for selected speed, torque and suspension load are performed. Second, these results are carried to iron loss calculations.

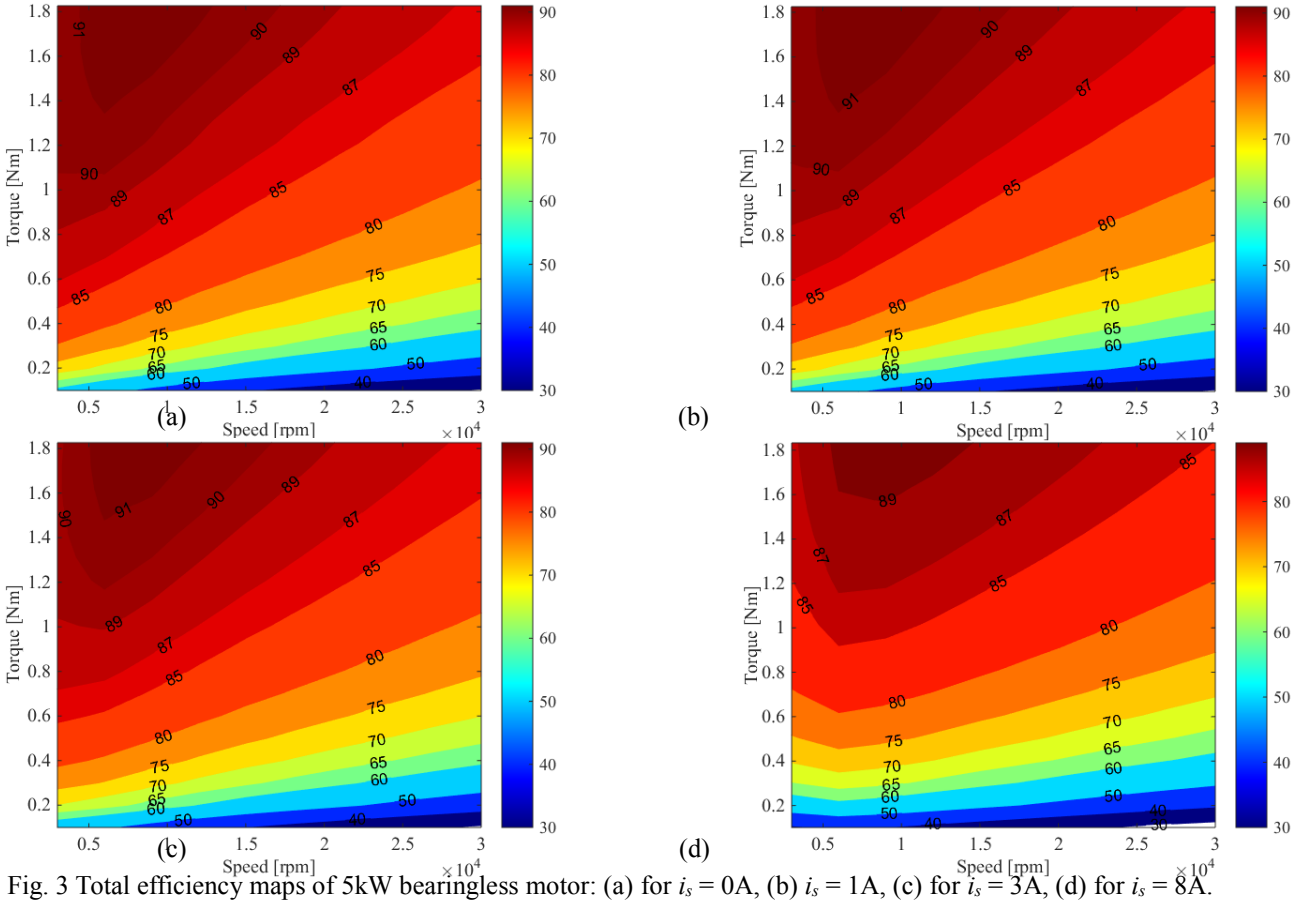

Fig. 3 Total efficiency maps of 5kW bearingless motor: (a) for i_s = 0A, (b) i_s = 1A, (c) for i_s = 3A, (d) for i_s = 8A.

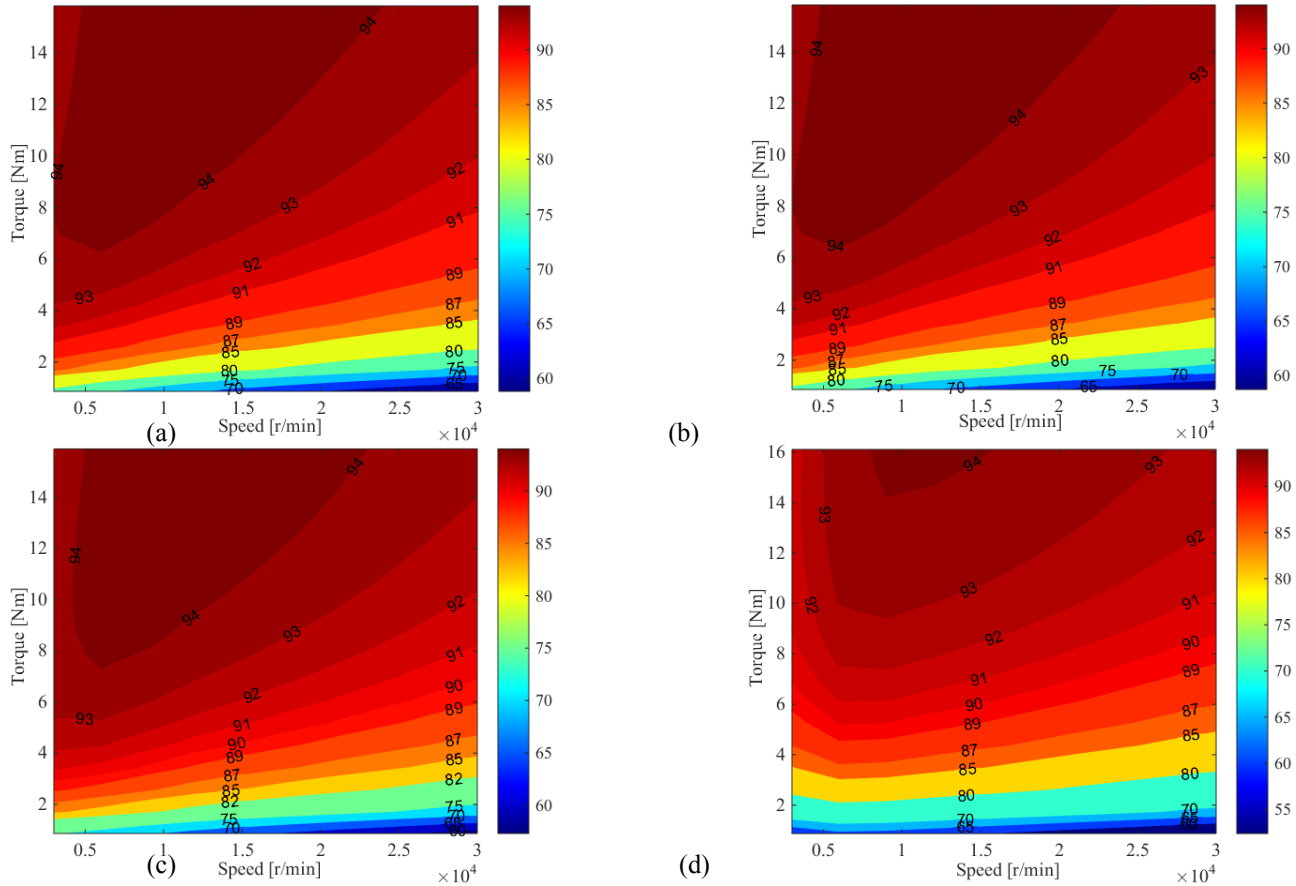

Fig. 4 Total efficiency maps of 50 kW bearingless motor: (a) for i_s = 0A, (b) for i_s = 1.8A, (c) for i_s = 6A, (d) for i_s = 24A.

The Joule, hysteresis and iron losses occurring in the stator and rotor are summed up with resistive, windage and additional losses of the machine. For high-speed operation windage losses are computed based on the accurate FEM rotor geometry for each disc and beam (as in Fig. 1 and Fig. 2) and for assumed working aerodynamic conditions. We use international civil aviation organization's (ICAO's) international standard atmosphere (ISA) or ISO 13443 reference conditions at 288.15 K and 101.325 kPa at 0 % relative humidity of air. For higher pressures where air-cooling is applied, the windage losses can increase considerably. The inverter losses are neglected. Finally, the total efficiency maps for particular rotor geometries are plotted. The constant suspension force vector has been assumed. The computations for first 64 harmonics and 180 points have been used for the each map because of computation load. Specifically the iron losses will be higher because of unaccounted harmonics and 3D effects. Therefore, some correction factor of about 1.7 for the iron, Joule and hysteresis losses is applied. The significant iron losses can be reduced by using better steel, e.g. JNHF-Core by JFE.

Figure 3 shows the total efficiency maps including magnetic suspension losses of 5 kW prototype bearingless motor for different suspension loading and when only q-direction motor current is applied. Figure 4 shows the equivalent efficiency maps of 50 kW motor unit. Both prototypes exhibit very high efficiency for its power rating. The suspension currents in the cases (b) in Fig. 3 and Fig. 4 are sufficient for overcoming the effects of gravity. The suspension currents in the cases (c) provide more realistic loading equal to three times the gravity loading. The total efficiency decrease about 1 % when the suspension reaches its design maximum in the cases (d). On one hand, the suspension current introduces additional losses. On the other hand, the presence of the suspension current and the motor current simultaneously enforces both the output torque and the output suspension force. The peak current values (amplitudes) are considered in the figures.

Figure 6 shows the losses distribution for the maximum loading torque. Especially the rotor losses increase when the suspension current is present. The contribution of the windage losses to the total losses is significantly greater for the 5 kW prototype compared to the 50 kW prototype.

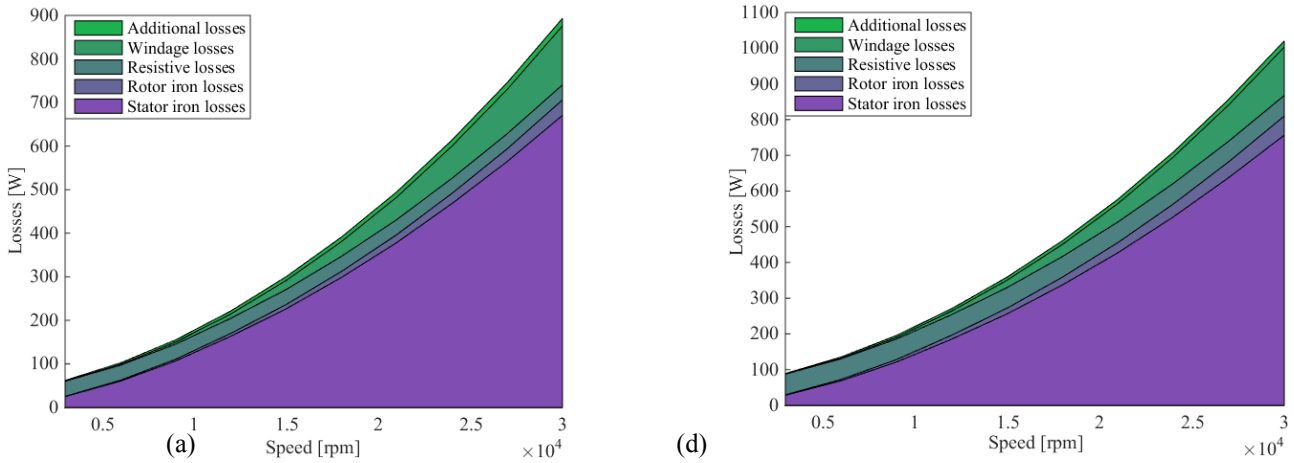

Fig. 5 Losses for the maximum loading torque of 5kW prototype for peak suspension currents: (a) i_s = 0A, (d) for i_s = 8A.

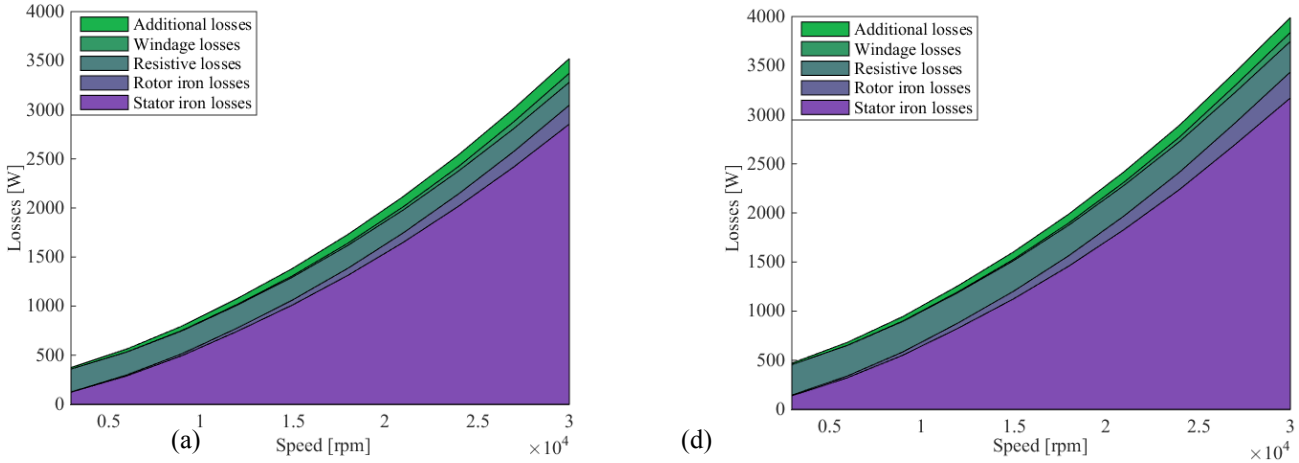

Fig. 6 Losses for the maximum loading torque of 50 kW motor for peak suspension currents: (a) i_s = 0A, (d) for i_s = 24A.

The second rotor has higher power density in respect to the rotor size. The efficiency maps are the same for the motor and for the generator operation. However, power factor maps slightly differ. Figure 7 and Figure 8 present the power factor maps for the both case study motors. The power factor for the motor windings are close to 1 while the power factors for the suspension windings are between 0.08 and 0.22. This reflects that the main function of the suspension current is not about performing work in time but in this case to produce static magnetic levitation force.

4. Computation of inductance map

The inductances are computed as the flux difference divided by the current, e.g. $L_{mq}=(\Phi_q\,(angle,i_q)-\Phi_q\,(angle,i_q=0))/i_q$, from the peak values of fluxes Φ and currents. Figure 9 and Figure 10 present the computed motor inductance maps.

The ABB's ACSM1 motion control drive has identified the 5kW motor (Figure 11) inductance values with the rotor supported on the mechanical bearings for commissioning as: L_{mq} = 0.97 mH and L_{md} = 0.91 mH. The preliminary identification using the specially designed an ID rig gave L_{mq} = 0.995 mH and L_{md} = 0.9997 mH. However, the exact rotor angle has been unknown during these measurements. The differences between the FEM computed inductance values and the measured inductances of the machine could result from the different actual airgap, flux leakages, and 3D effects. It is interesting to notice the effect of the rotor angle on the inductance values. The 24th cogging pattern can be noticed in the 5 kW prototype. The 12th cogging pattern can be noticed in the 50 kW prototype, which uses one slot pitch skew to smooth the flux in the airgap. In the case of the 50 kW motor the inductance surfaces have less variations because of skew. For the both motors, the presence of suspension current affects the inductances. With the suspension current, the inductance surfaces exhibit a pattern corresponding to 4-pole rotor structure.

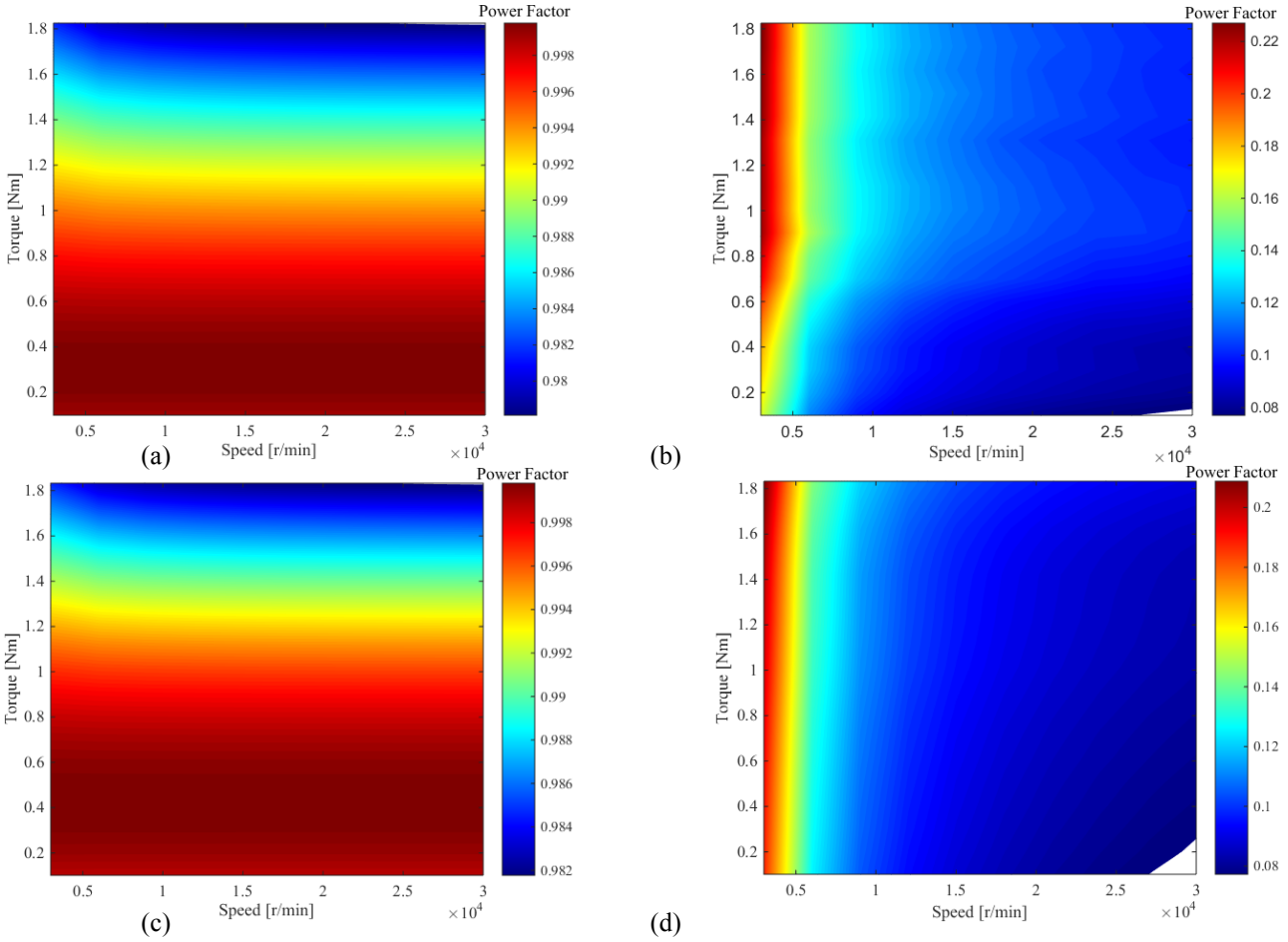

Fig. 7 Power factor of 5 kW motor: (a) for motor windings and i_s = 1 A, (b) for suspension windings and i_s = 1 A, (c) for motor windings and i_s = 8 A, (d) for suspension windings and i_s = 8 A.

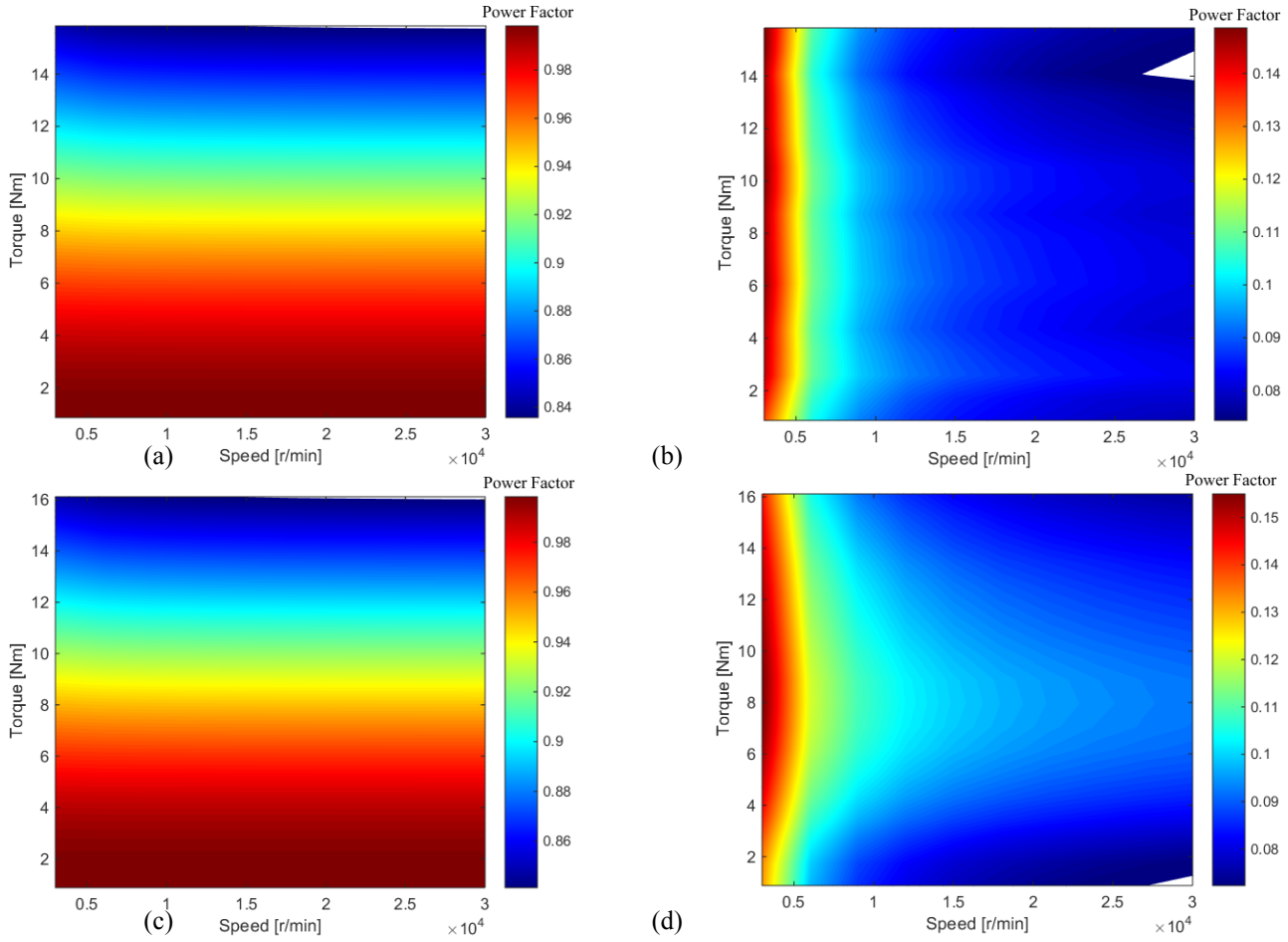

Fig. 8 Power factor of 50 kW prototype: (a) for motor windings and i_s = 1.8 A, (b) for suspension windings and i_s = 1.8A, (c) for motor windings and i_s = 24 A, (d) for suspension windings and i_s = 24 A.

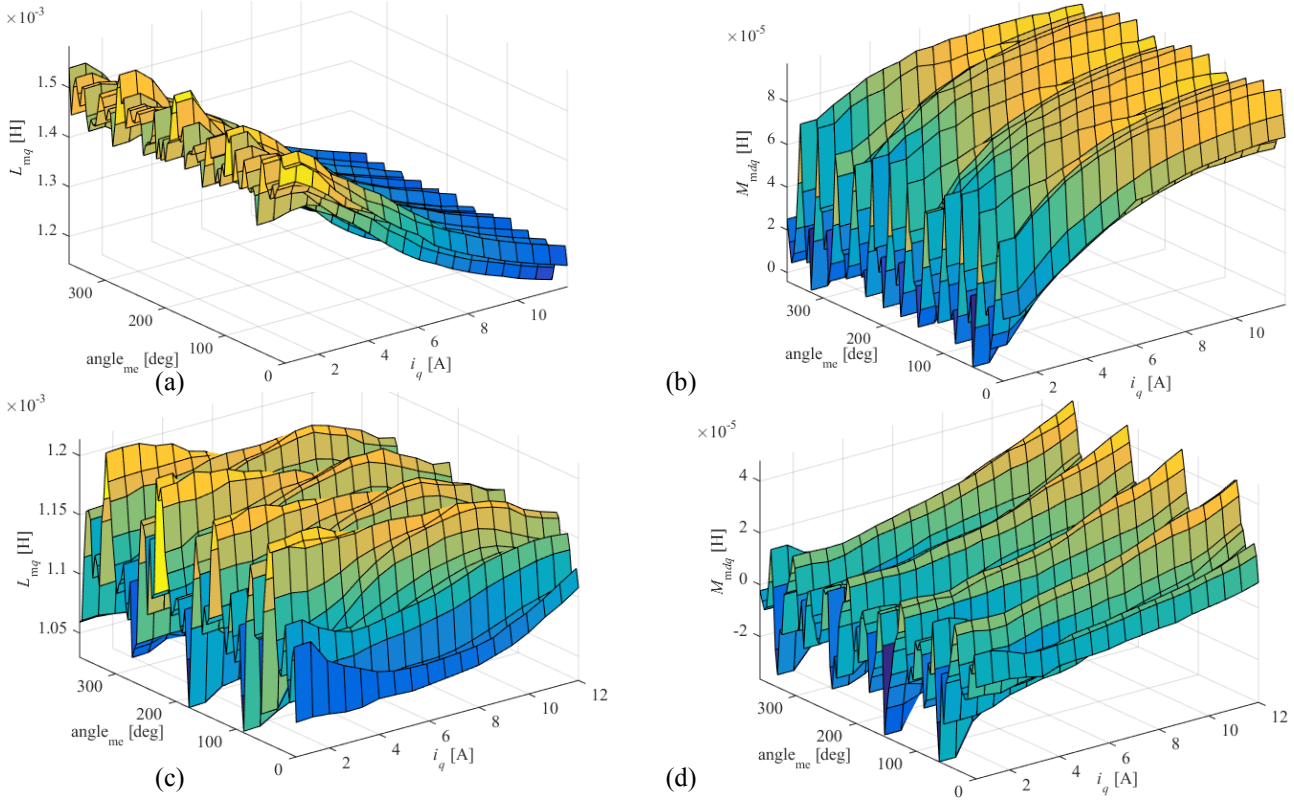

Fig. 9 Inductance maps of 5 kW motor: (a) L_{mq} for i_s = 1A, (b) M_{mdq} for i_s = 1A, (c) L_{mq} for i_s = 8A, (b) M_{mdq} for i_s = 8A.

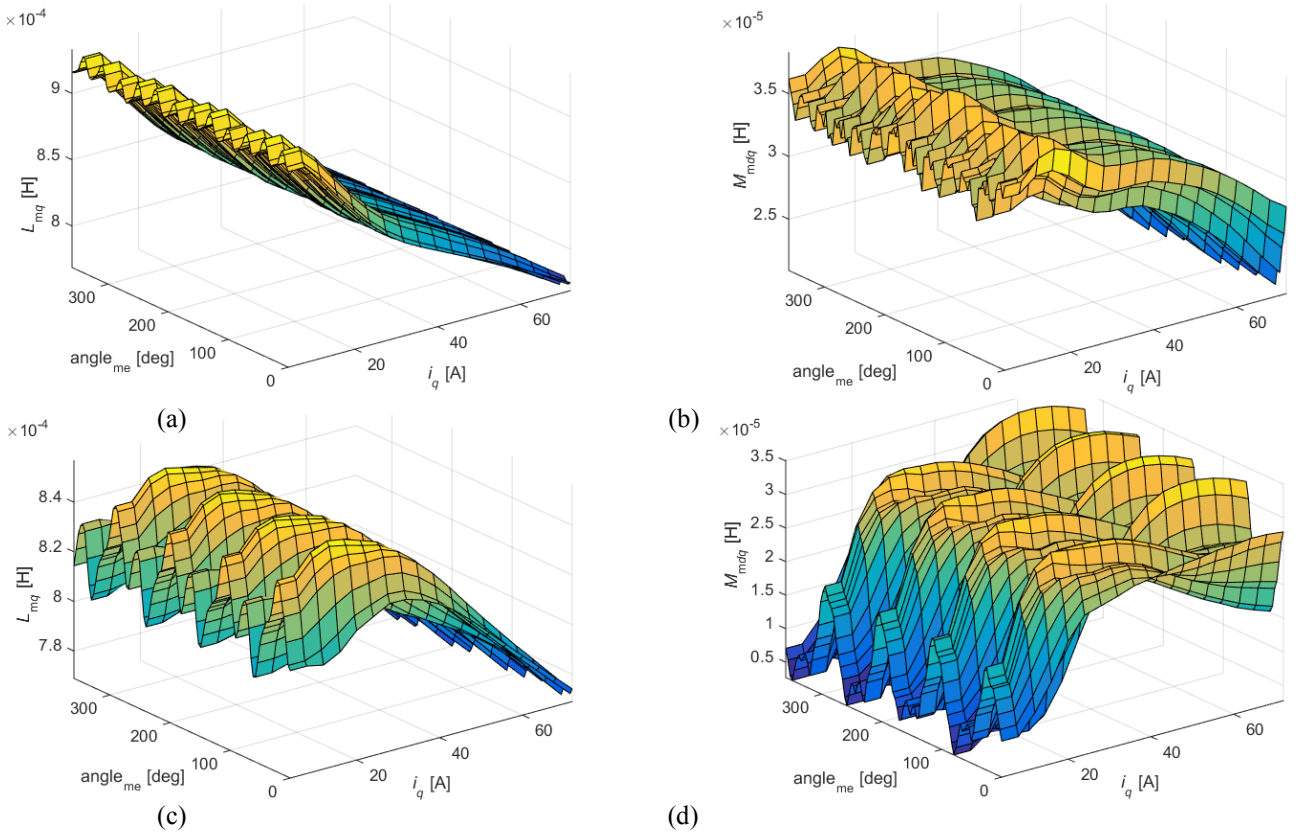

Fig. 10 Inductance maps of 50 kW prototype: (a) L_{mq} for i_s = 1.8 A, (b) M_{mdq} for i_s = 1.8 A, (c) L_{mq} for i_s = 24 A, (b) M_{mdq} for i_s = 24 A. The calculation takes into consideration a 15° skew in the stator.

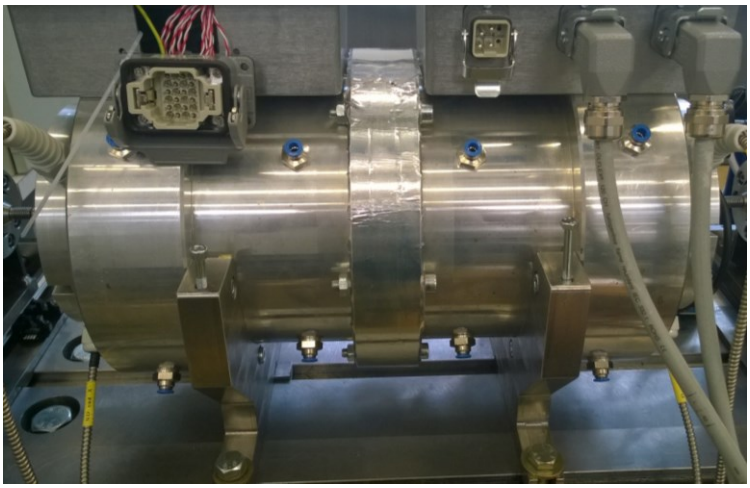

Fig 11 10 kW twin (2·5 kW) unit bearingless IPM motor prototype.

5. Conclusions

The total efficiency maps of the 4-pole motor and 2-pole suspension high-speed motors at different loading conditions were shown. For the static suspension loads, up to 3.5 times the total gravity force needed for the rotor suspension, the motor efficiencies are not affected by the magnetic suspension. Two studied motor designs have high efficiency over a wide operating range. The 5 kW machine has lower power density than the 50 kW unit. The power factors and inductances at different operating points were analyzed. The inductance variations can be used in uncertainty modelling and control design. With the higher loads, the efficiency slightly decreases. The performance of the 5 kW motor unit is currently undergoing experimental verification while the 50 kW unit is under construction at LUT.

Acknowledgment

The work has been co-funded by Academy of Finland No. 270012 and No. 273489.

References

Asama, J., Takemoto, M., Sugimoto, H., and Chiba, A., Performance Investigation and Power Factor Improvement of a Consequent-Pole Type Bearingless Motor. In Proc. of ISMB13 (2012), pp. 1–8.

Huynh, C., Zheng, L., and Acharya, D., Losses in High Speed Permanent Magnet Machines Used in Microturbine Applications, Journal of Engineering for Gas Turbines and Power, Vol. 131, No. 2 (2009), pp. 022301 1–6.

Jaatinen P., Jastrzebski R.P., Sugimoto H. Pyrhönen, O., Chiba, A., Optimization of the rotor geometry of a high-speed interior permanent magnet bearingless motor with segmented magnets, in Proc. of 18th International Conference on Electrical Machines and Systems (ICEMS) (2015), pp. 962–967.

Jastrzebski, R.P. Jaatinen, P. Sugimoto, H., Pyrhönen, O., Chiba, A., Design of a bearingless 100 kW electric motor for high-speed applications, in Proc. of 18th International Conference on Electrical Machines and Systems (ICEMS) (2015), pp. 2008–2014.

Munteanu, G., Binder, A., and Schneider, T., Loss measurement of a 40 kW high-speed bearingless PM synchronous motor, IEEE Energy Conversion Congress and Exposition, Issue 6 (2011), pp. 722–729.

Sergeant, P., and Van Den Bossche, A.P.M., Influence of the amount of permanent-magnet material in fractional-slot permanent-magnet synchronous machines, IEEE Transactions on Industrial Electronics, Vol. 61, No. 9 (2014), pp. 4979–4989.

Sinervo, A., and Arkkio, A., Rotor radial position control and its effect on the total efficiency of a bearingless induction motor with a cage rotor, IEEE Transactions on Magnetics, Vol. 50, No. 4 (2014). pp. 1–9.

Steinert, D., Nussbaumer, T., and Kolar, J.W., Slotless Bearingless Disk Drive for High-Speed and High-Purity Applications, IEEE Transactions on Industrial Electronics, Vol. 61, No. 11 (2014), pp. 5974–5986.

Yajima, S., Takemoto, M., Tanaka, Y., Chiba, A., and Fukao, T., Total efficiency of a deeply buried permanent magnet type bearingless motor equipped with 2-pole motor windings and 4-pole suspension windings, IEEE Power Engineering Society General Meeting (PES) (2007), pp. 1–7.